

# Saturation of Elliptic Flow and the Transport Opacity of the Gluon Plasma at RHIC

Dénes Molnár<sup>1,2</sup> and Miklos Gyulassy<sup>1,2,3</sup>

<sup>1</sup>*Physics Department, Columbia University, 538 W. 120th Street, New York, NY 10027*

<sup>2</sup>*RMKI Research Institute for Particle and Nuclear Physics, PO Box 49, H-1525 Budapest, Hungary*

<sup>3</sup>*Collegium Budapest, Szentháromság u. 2., H-1014 Budapest, Hungary*

(Received May 3, 2001)

Differential elliptic flow and particle spectra are calculated taking into account the finite transport opacity of the gluon plasma produced in Au+Au at  $E_{cm} \sim 130$  A GeV at RHIC. Covariant numerical solutions of the ultrarelativistic Boltzmann equation are obtained using the MPC parton cascade technique. For typical pQCD ( $\sim 3$  mb) elastic cross sections, extreme initial gluon densities,  $dN_g/d\eta \sim 15000$ , are required to reproduce the elliptic flow saturation pattern reported by STAR. However, we show that the solutions depend mainly on the transport opacity,  $\chi = \int dz \sigma_t \rho_g$ , and thus the data can also be reproduced with  $dN_g/d\eta \sim 1000$ , but with extreme elastic parton cross sections,  $\sim 45$  mb. We demonstrate that the spectra and elliptic flow are dominated by numerical artifacts unless parton subdivisions  $\sim 100 - 1000$  are applied to retain Lorentz covariance for RHIC initial conditions.

PACS 12.38.Mh; 24.85.+p; 25.75.-q

## I. INTRODUCTION

Differential elliptic flow,  $v_2(p_\perp) = \langle \cos(2\phi) \rangle_{p_\perp}$ , the second Fourier moment of the azimuthal momentum distribution for fixed  $p_\perp$ , is one of the important experimental probes of collective dynamics in  $A + A$  reactions [1–13]. The discovery [14] of a factor of two enhancement of elliptic flow in noncentral nuclear collisions at RHIC relative to SPS [15] has generated even more interest in this “barometric” measure of collective transverse flow. In addition, preliminary STAR data reported in [16] suggest a remarkable saturation property of this flow at high  $p_\perp$  with  $v_2(p_\perp > 2 \text{ GeV}) \sim 0.15$ . This corresponds to a factor of two azimuthal angle asymmetry of high- $p_\perp$  particle production relative to the reaction plane. This collective effect depends strongly on the dynamics in a heavy ion collision and therefore provides important constraints about the density and effective energy loss of partons. In particular, we show that it constrains the transport opacity of the produced gluon plasma.

Predictions of collective elliptic flow in noncentral nuclear collisions were first based on ideal (nondissipative) hydrodynamics [1,2,6]. Unlike at lower energies, ideal hydrodynamics seems to reproduce the (low  $p_T < 2$  GeV) data [14] at RHIC remarkably well. However, it fails to saturate at high  $p_\perp > 2$  GeV as indicated by the preliminary data [16]. The hydrodynamic results was found in [6] to be surprisingly insensitive to the choice of ini-

tial conditions, equation of state and freezeout criteria, once the observed  $dN_{ch}/d\eta$  was reproduced, leaving no adjustable hydrodynamic model parameters with which the saturation property could be reproduced.

The lack of saturation in ideal hydrodynamics is of course due to the assumption that local equilibrium can be maintained until a sudden freezeout hypersurface is reached. This idealization is certainly invalid outside some finite domain of phase space in heavy ion collisions [17]. Finite quantum transition rates are expected to produce nonequilibrium deviations from the predicted hydrodynamic flow pattern. Covariant Boltzmann transport theory provides a convenient framework to estimate dissipative effects. The assumption of local equilibrium is replaced by the assumption of a finite local mean free path  $\lambda(s, x) \equiv 1/\sigma(s)n(x)$ . The theory then naturally interpolates between free streaming ( $\lambda = \infty$ ) and ideal hydrodynamics ( $\lambda = 0$ ).

The previous calculations of collective flow from covariant transport theory [9,18,19] lead to too small collective effects. This was due to the use of small perturbative QCD cross sections and dilute parton initial densities based on HIJING [20]. Recently, denser parton initial conditions were suggested based on gluon saturation models [21]. Initial gluon densities up to five times higher than from HIJING were predicted. The question studied in this paper is whether such initial conditions may be dense enough to generate the observed collective flow even with pQCD elastic cross sections. In this paper, we explore the dependence of differential elliptic flow on initial conditions, or equivalently<sup>1</sup>, on the magnitude of partonic cross section.

We note that hadronic cascade models supplemented with string dynamics [4,10,11] also in general underpredict elliptic flow because the spatial asymmetry is too small after hadronization to generate the observed momentum space asymmetry. The reason is that hadronization through longitudinal string excitations reduces the strength of partonic level elliptic flow. To produce sufficient elliptic flow in string models, other mechanisms may have to be included such as colour exchange [10].

The saturation and eventual decrease of  $v_2$  at high

---

<sup>1</sup> The equivalence is due to the scaling property explained in Section II B.

$p_\perp$  has been predicted as a consequence of inelastic parton energy loss [12,13]. Those predictions however assumed the validity of an Eikonal approach at moderate  $p_T \sim 10$  GeV. In addition, the pQCD computable jet quenched part had to be joined phenomenologically onto a parametrized “soft” nonperturbative component below  $p_T < 2$  GeV/c. Covariant transport theory overcomes the need to treat soft and hard dynamics on different footings. It is the only practical self-consistent theoretical tool at present to address simultaneously both the soft collective component and the far from equilibrium high- $p_\perp$  component. While current parton cascade techniques lack at present a *practical* means to implement covariant inelastic energy loss, it is of considerable theoretical interest to solve covariant Boltzmann theory even in the elastic limit since so few solutions are known. We solve that theory numerically here to get insight into the dynamical interplay between the soft and hard components over a wide dynamical range of parameters.

For large enough elastic opacities, the observed collective flow strength can certainly be reproduced [19]. The outstanding question which we focus on is whether the detailed pattern of deviations from ideal hydrodynamic flow and its saturation at high  $p_\perp$  can also be understood quantitatively in this particular dynamical framework.

Forerunners of this study [9,19] computed elliptic flow for partonic systems starting from initial conditions expected at RHIC. In this paper we extend those studies in three aspects. We compute the  $p_\perp$ -differential elliptic flow  $v_2(p_\perp)$ . The consequences of hadronization are investigated, which is necessary to compare to the observations. Finally, we use realistic diffuse nuclear geometry for the initial conditions.

We compute the partonic evolution with MPC [22], a newly formulated, covariant, parton kinetic theory technique. MPC is an extension of the covariant parton cascade algorithm, ZPC [23]. Both MPC and ZPC have been extensively tested [24,25] and compared to analytic transport solutions and covariant Euler and Navier-Stokes dynamics in 1+1D geometry. A critical feature of both these algorithms is the implementation of the parton subdivision technique proposed by Pang [25,26].

Extensions of MPC to include inelastic  $2 \leftrightarrow 3$  partonic processes [18] are under development. In this paper, we apply MPC in the pure elastic parton interactions mode as in ZPC [27].

## II. COVARIANT TRANSPORT THEORY

### A. Transport equation

We consider here, as in Refs. [26,23,22,17], the simplest but nonlinear form of Lorentz-covariant Boltzmann transport theory in which the on-shell phase space density  $f(x, \mathbf{p})$ , evolves with an elastic  $2 \rightarrow 2$  rate as

$$p_1^\mu \partial_\mu f_1 = \iiint_{234} (f_3 f_4 - f_1 f_2) W_{12 \rightarrow 34} \delta^4(p_1 + p_2 - p_3 - p_4) + S(x, \mathbf{p}_1). \quad (1)$$

Here  $W$  is the square of the scattering matrix element, the integrals are shorthands for  $\int_i \equiv \int \frac{g d^3 p_i}{(2\pi)^3 E_i}$ , where  $g$  is the number of internal degrees of freedom, while  $f_j \equiv f(x, \mathbf{p}_j)$ . The initial conditions are specified by the source function  $S(x, \mathbf{p})$ , which we discuss later in Section III.

For our applications below, we interpret  $f(x, \mathbf{p})$  as describing an ultrarelativistic massless gluon gas with  $g = 16$  (8 colors, 2 helicities). We neglect quark degrees of freedom because at RHIC gluons are more abundant.

In principle, the transport equation (1) could be extended for bosons with the substitution  $f_1 f_2 \rightarrow f_1 f_2 (1 + f_3)(1 + f_4)$  and a similar one for  $f_3 f_4$ . In practice, no covariant algorithm yet exists to handle such nonlinearities. We therefore limit our study to quadratic dependence of the collision integral on  $f$ .

The elastic gluon scattering matrix elements in dense parton systems are modeled by a Debye-screened form

$$\frac{d\sigma}{dt} = \sigma_0 \left(1 + \frac{\mu^2}{s}\right) \frac{\mu^2}{(t + \mu^2)^2}, \quad (2)$$

where  $\mu$  is the screening mass,  $\sigma_0 = 9\pi\alpha_s^2/2\mu^2$  is the total cross section, which we chose to be independent of energy. For small values of  $\mu$ , forward-peaked scattering is favored, while as  $\mu$  increases the angular distribution becomes more and more isotropic. For a fixed total cross section<sup>2</sup>, the relevant transport cross section is

$$\sigma_t(s) \equiv \int d\sigma_{el} \sin^2 \theta_{cm} = \int dt \frac{d\sigma_{el}}{dt} \frac{4t}{s} \left(1 - \frac{t}{s}\right) = \sigma_0 4z(1+z) [(2z+1) \ln(1+1/z) - 2], \quad (3)$$

where  $z \equiv \mu^2/s$ . This is a monotonic function of  $\mu$  and maximal in the isotropic ( $\mu \rightarrow \infty$ ) case. In the small angle dominated limit, with  $z \ll 1$ ,  $\sigma_t/\sigma_0 \approx 4z(\ln 1/z - 2)$ .

It is important to emphasize that while the cross section suggests a geometrical picture of action over finite distances, we use Eq. (2) only as a convenient parametrization to describe the effective *local* transition probability,  $W$ . In the present study this is simply modeled as  $dW/dt = s d\sigma/dt$ . The particle subdivision technique (see next Subsection) needed to recover covariance removes all notion of nonlocality in this approach, just like in hydrodynamics. Thus, the cross sections, e.g., 100 mb, used in the present study to simulate a high collision rate do *not* imply acausal action at a distance.

<sup>2</sup> To keep the total cross section constant as a function  $\mu$ , one of course has to adjust the coupling  $\alpha_s$  accordingly.

## B. Parton Subdivision

We utilize the parton cascade method to solve the Boltzmann transport equation (1). A critical drawback of all cascade algorithms is that they inevitably lead to numerical artifacts that violate Lorentz covariance. This occurs because particle interactions are simulated to occur whenever the distance of closest approach (in the relative c.m.) is  $d < \sqrt{\sigma_0/\pi}$ .

Acausal (superluminal) propagation due to action at a distance leads to severe numerical artifacts. In particular, the transverse energy evolution  $dE_t(\tau)/dy$  and the final asymptotic transverse energy per unit rapidity are frame dependent [17].

To recover the *local* character of equation (1) and hence Lorentz covariance, it is essential to use the parton subdivision technique [26,23]. This technique is based on the covariance of Eq. (1) under the transformation

$$f \rightarrow f' \equiv \ell f, \quad W \rightarrow W' \equiv W/\ell \quad (\sigma \rightarrow \sigma' = \sigma/\ell), \quad (4)$$

where  $\ell$  is the number of particle subdivisions. The magnitude of numerical artifacts is governed by the diluteness of the system  $\sqrt{\sigma}/\lambda_{MFP}$ , which scales with  $1/\sqrt{\ell}$  [25]. Lorentz violation therefore formally vanishes in the  $\ell \rightarrow \infty$  limit. In practice, very high  $\sim 100 - 1000$  subdivisions are needed [17] to obtain accurate numerical solutions of the transport equation (1) for initial conditions expected at RHIC.

## C. Scaling of the transport solutions

Subdivision covariance (4) actually implies that the transport equation has a broad dynamical range, and the solution for any given initial condition and transport property immediately provides the solution to a broad band of suitably scaled initial conditions and transport properties. This is because solutions for problems with  $\ell$  times larger the initial density  $dN/d\eta d^2x_\perp$ , but with one  $\ell$ -th the reaction rate can be mapped to the original ( $\ell = 1$ ) case for *any*  $\ell$ . We must use subdivision to eliminate numerical artifacts. However, once that is achieved, we have actually found the solution to a whole class of suitably rescaled problems.

The dynamical range of the transport equation (1) is further increased by its covariance under coordinate and momentum rescaling [17], leading to covariance of the transport theory under

$$\begin{aligned} f(x, \mathbf{p}) &\rightarrow f'(x, \mathbf{p}) \equiv \ell_p^{-3} \ell f\left(\frac{x}{\ell_x}, \frac{\mathbf{p}}{\ell_p}\right), \\ W(\{p_i\}) &\rightarrow W'(\{p_i\}) \equiv \frac{\ell_p^2}{\ell_x \ell} W\left(\left\{\frac{p_i}{\ell_p}\right\}\right), \\ m &\rightarrow m' = m/\ell_p, \end{aligned} \quad (5)$$

where  $\ell_x$  and  $\ell_p$  are the coordinate and momentum scaling parameters, respectively. This means [17] that we

can scale one solution to others provided that both  $\mu/T_0$  and  $\sigma_0 dN/d\eta$  remain the same (we cannot exploit coordinate scaling because the nuclear geometry is fixed). For example, three times the density with one-third the cross section leaves both parameters the same, hence the results can be obtained via scaling without further computation.

In general the numerical (cascade) solution of Eq. (1) tends in the  $\ell \rightarrow \infty$  limit toward a covariant physical solution that depends on two scales,  $\mu/T_0$  and  $\sigma_0 dN/d\eta$ . In an Eikonal picture of high- $p_\perp$  production, the distributions are expected to depend on the opacity or the mean number of collisions in the medium

$$\begin{aligned} \langle n \rangle &= \frac{L}{\lambda_{el}} = \int dt \frac{d\sigma_{el}}{dt} \int dz \rho\left(z, \tau = \frac{z}{c}\right) \\ &\approx \frac{dN}{dy} \frac{\sigma_{el}}{2\pi R_G^2} \log \frac{R_G}{\tau_0}, \end{aligned} \quad (6)$$

where  $\tau_0$  is the formation proper time and  $R_G$  is the effective Gaussian transverse coordinate rms radius.

However, from the point of view of dissipative dynamics via Navier-Stokes and Fokker-Planck equation, the more relevant dynamical parameter is the effective *transport opacity*

$$\chi \equiv \frac{\sigma_t}{\sigma_{el}} \langle n \rangle = \sigma_t \langle \int dz \rho(\mathbf{x}_0 + z\hat{n}, \tau = \frac{z}{c}) \rangle. \quad (7)$$

The ensemble average over initial coordinates and directions is implied above. In addition,  $\sigma_t$  here stands for  $\sigma_t \equiv \sigma_t(\langle s \rangle)$ , where  $\langle s \rangle = 18T_0^2$  is the initial thermal average of  $s$ . This is an approximation to the ensemble average  $\langle \sigma_t(s) \rangle$ .

In general, the transport opacity is a dynamical quantity that we do not know until we solved the transport equation for the set of parameters  $b$ ,  $\sigma_0 dN(0)/d\eta$ , and  $\sigma_t/\sigma_0$  (or equivalently,  $\mu/T_0$ ). However, as we can see from Table I, for the range of parameters considered in this study it is (within 10% accuracy) proportional to the product of the two scales  $\sigma_0 dN(0)/d\eta$  and  $\sigma_t/\sigma_0$ :

$$\chi(b, \sigma_0 \frac{dN(0)}{d\eta}, \frac{\sigma_t}{\sigma_0}) \approx \text{const} \times \sigma_t \frac{dN(0)}{d\eta} C(b). \quad (8)$$

The nontrivial, impact parameter dependent part  $C(b)$  is the number of collisions per parton as a function of  $b$  with  $\sigma_0 dN(0)/d\eta$  and  $\mu/T_0$  kept fixed. It is tabulated, for example, in section E) in Table I, in which case the corresponding proportionality constant is  $(\sigma_t dN(0)/d\eta)^{-1} = (0.91 \text{ mb} \times 210)^{-1}$ .

Of course, there is no a priori guarantee that the solutions of Eq. (1) depend only on this transport opacity parameter. However, as we will demonstrate numerically below, this turns out to hold within  $\sim 10 - 20\%$  accuracy for elliptic flow and the transverse momentum spectra out to 6 GeV/c for the parameters and initial conditions appropriate at RHIC energies.

### III. NUMERICAL RESULTS FOR THE PARTONIC EVOLUTION

In this Section we present elliptic flow results and  $p_\perp$  spectra for the partonic evolution.

Under the scaling (5) the differential elliptic flow  $v_2(p_\perp)$  and the  $p_\perp$  spectrum transform as

$$v_2(p_\perp) \rightarrow v_2'(p_\perp) \equiv v_2\left(\frac{p_\perp}{\ell_p}\right)$$

$$\frac{dN}{d^2p_\perp}(\mathbf{p}_\perp) \rightarrow \frac{dN'}{d^2p_\perp}(\mathbf{p}_\perp) = \ell \frac{dN}{d^2p_\perp}\left(\frac{\mathbf{p}_\perp}{\ell_p}\right). \quad (9)$$

Hence elliptic flow depends on  $\sigma_t$  and  $dN/d\eta$  only through the product  $\sigma_t dN/d\eta$ . On the other hand, the  $p_\perp$  spectrum depends on  $\sigma_t$  and  $dN/d\eta$  separately.

For Au+Au collisions, the initial condition was taken to be a longitudinally boost invariant Bjorken tube in local thermal equilibrium at temperature  $T_0$  at proper time  $\tau_0 = 0.1$  fm/c with uniform pseudorapidity  $\eta \equiv 1/2 \log((t+z)/(t-z))$  distribution between  $|\eta| < 5$ . The transverse density distribution was assumed to be proportional to the binary collision distribution for two Woods-Saxon distributions. For collisions at impact parameter  $b$  the transverse binary collision profile is

$$\frac{dN(\mathbf{b})}{d\eta d^2\mathbf{x}_\perp} = \sigma_{jet} T_A\left(\mathbf{x}_\perp + \frac{\mathbf{b}}{2}\right) T_A\left(\mathbf{x}_\perp - \frac{\mathbf{b}}{2}\right), \quad (10)$$

where  $T_A(\mathbf{b}) \equiv \int dz \rho_A(\sqrt{z^2 + \mathbf{b}^2})$ , in terms of the diffuse nuclear density  $\rho_A(r)$ . The pQCD jet cross section normalization,  $\sigma_{jet}$ , and the temperature  $T_0$  were determined by fitting the gluon minijet transverse momentum spectrum predicted by HIJING [20] for central Au+Au collisions at  $\sqrt{s} = 130A$  GeV (without shadowing and jet quenching). This gives  $dN(0)/d\eta = 210$  and  $T_0 = 700$  MeV.

Evolution from different initial densities (but the same density profile) can be obtained by varying the cross section only and using the scaling property explained in Section II C.

The evolution was performed numerically with 40 and 100 mb isotropic cross sections, and with 3, 40 and 100 mb gluonic cross sections with  $\mu/T_0 = 1$ . We used particle subdivision  $\ell = 100$  for impact parameters 0, 2, and 4 fm, while  $\ell = 220, 450, 1100$ , and 5000, for  $b = 6, 8, 10$ , and 12 fm.

As emphasized in the previous Section, we will label the results by the effective elastic transport opacity  $\chi$  from Eq. (7) and the impact parameter  $b$ . Table I shows  $\chi$  for each simulation, determined directly from the average number of cascade collisions per particle. In Table I we also introduced letter codes A) through F) as a quick reference to particular subsets of simulation parameters. We will include this letter code on most labels together with  $\chi$ , for convenience.

### A. Elliptic flow results

Figures 1 and 2 show the final asymptotic gluon elliptic flow as a function of transverse momentum for different impact parameters. With increasing  $p_\perp$ , elliptic flow increases until  $p_\perp \sim 1.5 - 2$  GeV, where it saturates, reproducing the pattern observed at RHIC. With increasing impact parameter, elliptic flow first monotonically increases, then monotonically decreases, showing a maximum at  $b \approx 8$  fm. These features were universal for all the cross sections we studied. Also, as expected, elliptic flow is a monotonically increasing function of the transport opacity, if the impact parameter is kept fixed.

Figure 3 shows the  $p_\perp$ -integrated gluon elliptic flow as a function of centrality. The cascade reproduces the trend seen in the STAR data down to very small centralities  $\sim 0.1 - 0.2$ , where the ideal hydrodynamical assumption of zero mean free path certainly breaks down. To *quantitatively* reproduce the data, transport opacities  $\chi_{b=0} \sim 4 - 7$  are needed. With the pQCD elastic  $gg$  cross section  $\sigma_0(\mu = T) \approx 3$  mb, this corresponds to an initial gluon density  $dN_g(0)/d\eta \sim 3000 - 5000$ .

Figure 4 shows the impact-parameter-averaged gluon elliptic flow as a function of transverse momentum for different transport opacities. The impact-parameter-averaged flow was computed via the formula

$$v_2^{av}(p_\perp) \equiv \frac{2\pi}{\pi b_{max}^2} \int_0^{b_{max}} db b \frac{\int d\phi \cos(2\phi) \frac{dN}{d\eta d^2p_\perp}(b)}{\int d\phi \frac{dN}{d\eta d^2p_\perp}(b)}, \quad (11)$$

with  $b_{max} = 12$  fm. As we show in the Appendix, for our transport theory solutions, Eq. (11) gives comparable results to the minimum-bias differential elliptic flow defined by STAR as

$$v_2^{STAR}(p_\perp) \equiv \frac{\int_0^{b_{max}} b db \int d\phi \cos(2\phi) \frac{dN}{d\eta d^2p_\perp}(b)}{\int_0^{b_{max}} b db \int d\phi \frac{dN}{d\eta d^2p_\perp}(b)}, \quad (12)$$

which weights flow in more central events preferentially. This is not the case for ideal hydrodynamic solutions [6], for which the STAR definition results in much smaller flow than if Eq. (11) is used.

We use the definition (11) because it can be computed numerically more reliably in our approach. As discussed below, it is difficult to reduce cascade numerical artifacts to an acceptable level when the transport opacity  $\chi$  is large. For all other parameters kept fixed,  $\chi$  increases with decreasing impact parameter, hence the STAR definition that weights  $v_2$  at small  $b$  preferentially is more prone to such numerical artifacts.

Figure 5 shows that subdivision scaling (4), hence Lorentz covariance [17], is strongly violated for insufficient particle subdivision. For the initial conditions for Fig. 5 ( $b = 8$  fm,  $\chi = 4.87$ ), a particle subdivision  $\sim 200$  is needed to reduce numerical artifacts to a reasonable

level. This also means that for  $b = 0, 2, \text{ and } 4 \text{ fm}$ ,  $\ell = 100$  is not sufficient if  $\chi > 4 - 5$ . Unfortunately, our computational resources were insufficient to allow higher subdivision runs.

Varying the magnitude of energy loss we searched for the drop in  $v_2(p_\perp)$  at high  $p_\perp$  predicted by calculations based on parton energy loss [12,13]. Although those studies consider only effects due to radiative energy loss, one expects a similar behavior in case of purely elastic energy loss.

Figure 6 shows the dependence of  $v_2(p_\perp)$  on the transport opacity for a fixed impact parameter. We varied the opacity by changing the screening mass  $\mu$ . As expected, elliptic flow decreases with decreasing  $\chi$ . However, there is no sign of a drop at high  $p_\perp$ : within statistical errors, the results are consistent with a constant flow from 2 to 6 GeV transverse momentum.

## B. Particle spectra

Figures 7 and 8 show the final gluon  $p_\perp$  spectra as a function of transport opacity and impact parameter. While HIJING densities with the pQCD elastic cross section are too dilute ( $\chi \sim 0.01 - 0.1$ ) to produce more than  $\sim 10\%$  quenching, as we increase the transport opacity, quenching “turns on” and by  $\chi \sim 7 - 8$  it is an order of magnitude at  $p_\perp > 6 \text{ GeV}$ .

Figure 11 shows that, unlike elliptic flow which is also driven by the spatial anisotropy, the relevant parameter that governs quenching is  $\chi$  alone. With 20% accuracy, simulations with very different impact parameters agree on the magnitude of quenching, provided  $\chi$  is the same.

While the quenching depends on  $\chi$  only, the absolute yield is proportional to the initial  $dN/d\eta$ . Hence from the absolutely normalized measured spectrum at a given centrality one could extract both  $\sigma_t$  and  $dN(0)/d\eta$ .

The  $p_\perp$  spectra are very sensitive to particle subdivision, as shown in Fig. 10. For insufficient subdivision, the high- $p_\perp$  spectrum is “reheated” during the expansion, which is clearly a numerical artifact. As the subdivision is increased, “reheating” disappears and, for the particular parameters ( $b = 8 \text{ fm}$ ,  $\chi = 4.87$ ), the spectrum converges for  $\ell \sim 250$ .

## C. Transport opacity dependence

In this Section we provide numerical evidence for the remarkable invariance of the results on the actual angular dependence of the differential cross section (2). Only the transport cross section moment (3) seems to matter for the problem considered here as seen from Fig. 11.

The reason that this simplification occurs is that for the  $\mu$  and gluon energy range considered in these plots, the transport opacity is actually high enough that little memory of the *initial* gluon momentum direction remains

after multiple scattering. Thus, isotropic scattering and  $\mu = T$  forward scattering both lead to essentially a random reorientation of all the gluons involved.

To see this in detail, we show in Fig. 13 that aside from a small 10% delta function component due to the gluons in the “corona” surface region that escape without rescattering, the bulk of the minijets undergo enough rescatterings that their final direction is randomized. In Fig. 12 we show that the rapidity shift of gluons in each transverse momentum interval considered has the form close to one expected if local thermal equilibrium occurred:

$$\begin{aligned} \frac{dP}{d\Delta y} &= \int dm_{\perp i}^2 dy_i dm_{\perp f}^2 m_{\perp i} \cosh y_i m_{\perp f} \cosh(y_i + \Delta y) \\ &\times \frac{1}{4T_i^3} \frac{1}{4T_f^3} e^{-(m_{\perp i} \cosh y_i)/T_i} e^{-[m_{\perp f} \cosh(y_i + \Delta y)]/T_f} \\ &= \frac{\Delta y \cosh \Delta y - \sinh \Delta y}{\sinh^3 \Delta y}. \end{aligned} \quad (13)$$

This final randomization of momenta is however not sufficient to ensure the validity of local equilibrium necessary for the applicability of nondissipative (Euler) hydrodynamics. This can be seen from the dependence of the transverse momentum spectra and elliptic flow on the *finite* opacity parameter itself. In the hydrodynamic limit  $\chi = \infty$  and as we showed in detail in a previous study [17], the solutions of the transport equations differ very much from ideal hydrodynamics. While no covariant 3+1D Navier-Stokes solutions are yet known, our transport solutions demonstrate the effects of dissipation through their dependence on  $1/\chi$ , which is effectively a measure of the importance of viscosity.

The invariance of the transport solutions to the angular distributions for a fixed  $\chi$  indicate however that we are not extremely far from the local thermal though dissipative limit. In particular, our high opacity solutions are far from the Eikonal (Knudsen) type dynamics as considered in [13].

A criterion for the validity of the Eikonal approximation is that the angle between the initial and final parton momenta satisfies  $\Delta\theta \ll 1$ , say  $\Delta\theta < 0.1$ . For an energetic parton that undergoes  $N$  elastic collisions, this angle can be approximated in an analogous way to random walk as

$$\langle \Delta\theta \rangle \approx \sqrt{\langle \sin^2 \Delta\theta \rangle} \approx \sqrt{N \langle \sin^2 \theta_{cm} \rangle} = \sqrt{\chi}, \quad (14)$$

where we used Eqs. (3) and (7) in the last step. Hence, for elastic collisions, Eikonal approximation is valid only for very small  $\chi < 0.01$  transport opacities. Even in the most optimistic  $N = 1$  case, this condition is satisfied only for  $z \equiv \mu^2/s < 4 \times 10^{-4}$ . For collisions with typical thermal partons ( $s \approx 6ET$ ,  $\mu = T$ ), this requires parton energies  $E > \sim 500T$ , i.e., several hundred GeV in our case.

Similar considerations hold for  $N > 1$  as well because the total cross section does not depend on the parton

energy and therefore the number of collisions is approximately independent of energy. In Fig. 13 we demonstrate that the Eikonal limit is approached very slowly as the parton energy increases. The trend is weak because the transverse momenta which are considered are orders of magnitude below the 100 GeV regime.

What we see with these results is that the pattern of “jet quenching”, as observed at RHIC via the suppression of moderate transverse momentum particles and the saturation of elliptic flow above some critical  $p_{\perp}$ , can be reproduced if sufficiently high transport opacities are postulated.

## IV. RESULTS FOR HADRONS

The results in the previous Section pertain to the partonic world. To compare with experimental results, we have to model hadronization. Here we compute the hadronic observables from two different hadronization schemes.

### A. Hadronization via local parton-hadron duality

A simple hadronization model can be constructed based on local parton-hadron duality. Following Ref. [21], we simply assume that each gluon gets converted to a pion with equal probability for the three isospin states. Since most hadrons are pions, we approximate the transverse momentum distribution of negative charged hadrons with that of the negative pions as

$$f_{h^-}(\mathbf{p}_{\perp}) \approx f_{\pi^-}(\mathbf{p}_{\perp}) = \frac{1}{3}f_g(\mathbf{p}_{\perp}). \quad (15)$$

With the above prescription, elliptic flow does *not* change during hadronization, i.e., Figs. 1–6 show the negative hadron flow as well. Furthermore, the negative hadron  $p_{\perp}$  spectra can be obtained from Figs. 7–10 via simply dividing by 3. Consequently, the scaling (9) holds for the negative hadron flow and spectra as well.

In Fig. 4, the elliptic flow data by STAR are reproduced with a transport opacity  $\chi_{b=0} = 23.9$ . For an initial gluon density  $dN_g(0)/d\eta = 1000$ , this corresponds to  $\sigma_t \approx 14$  mb, i.e., to a total cross section of  $\sigma_0 \approx 45$  mb with  $\mu = T_0$ . If we took the pQCD  $gg$  cross section of 3 mb with  $\mu = T_0$ , this opacity would correspond to an initial gluon density of  $dN_g(0)/d\eta \sim 15000$  that is contradicted by the much smaller observed  $dN_{ch}/d\eta \approx 600$ .

The  $p_{\perp}$  spectra provide a much stronger constraint on the initial gluon density as their absolute magnitude is proportional to it. At high opacities ( $\chi > \sim 5$ ), the need for high particle subdivisions poses a severe computational problem, therefore we can reliably compute particle spectra for semicentral collisions only. Nevertheless, the data measured by STAR in central collisions, where quenching due to parton energy loss is expected to be

maximal, provides an important lower bound on the particle yields. Figure 7 shows that the elastic transport opacities  $\chi < \sim 10$  considered here are compatible with this lower bound.

On the other hand, the cascade semicentral results seem to be too far above the central measurements. It is unlikely that going from semicentral to central collisions would give us an order of magnitude or more increase in quenching needed to reach the central STAR data. Either much higher opacities  $\chi \gg 10$  than those considered in this study would be needed to reach the central data, or it may even be that with this hadronization scheme it is not possible to reproduce the data even in the  $\chi \rightarrow \infty$  hydrodynamic limit.

### B. Hadronization via independent fragmentation

Another possible hadronization scheme is the fragmentation of gluons as independent jets. Since the majority of the hadrons are pions, we consider only the  $g \rightarrow \pi^{\pm}$  channel with the next-to-leading-order fragmentation function computed in Ref. [28]. We take the scale factor  $s \equiv \log(Q^2)/\log(Q_0^2)$  to be zero because the initial HIJING gluon distribution is already quenched due to initial and final state radiation. Also, since we do not consider soft physics, we limit our study to hadrons with  $p_{\perp} > 2$  GeV and hence fragment gluons with  $p_{\perp} > 2$  GeV only.

Figure 14 shows the final impact-parameter-averaged negative hadron flow as a function of the transport opacity. The flow pattern and the magnitude of the flow are much the same as for partons in Fig. 4. Hence, we get the same constraint on the initial parameters as for hadronization via local parton-hadron duality. In the  $p_{\perp} < 2$  GeV region this simple calculation does not reproduce the data because it does not include contributions coming from soft physics.

The  $p_{\perp}$  spectra of charged hadrons are shown as a function of transport opacity and impact parameter in Figs. 15 and 16. In addition to quenching because of energy loss, the final pion spectra are further quenched due to independent fragmentation. With this additional quenching, the parton cascade results approach the STAR data, as indicated in Fig. 17, for rather extreme  $\sigma_0(\mu = T) = 100$  mb if HIJING  $dN_g/dy = 210$  is assumed, or if  $\sigma_0 = 25$  mb and EKRT  $dN_g/dy = 1000$  is assumed. These elastic cross sections exceed the conventional few mb pQCD cross sections at this scale by at least an order of magnitude.

## V. CONCLUSIONS

The MPC parton cascade technique was applied to solve the covariant Boltzmann transport numerically and compute new observables at RHIC. Our focus was on the

preliminary differential elliptic flow and charged hadron moderate  $p_{\perp} > 2$  GeV/c spectra. We compared results using two different hadronization schemes: independent fragmentation and local parton-hadron duality.

Our main result is that if only elastic scattering is taken into account in the covariant Boltzmann equation, extremely large densities and/or elastic parton cross sections,  $\sigma_{tot}dN/d\eta \sim 80$  times the HIJING estimate, are needed to reproduce the elliptic flow data [16]. Hadronization via local parton-hadron duality fails to reproduce the rapidly falling high- $p_{\perp}$  spectra. However, independent fragmentation of our MPC solutions compare well to the charged hadron  $p_{\perp}$  spectra when rather large elastic transport opacities are postulated.

The solutions clearly demonstrate how finite (even extreme) reaction rates in  $A + A$  lead to major deviations from ideal hydrodynamic transverse flow effects at transverse momentum  $p_T > 2$  GeV. The pattern of quenching found with MPC is surprisingly similar to that obtained in the two component model of GVW [13]. The main difference between the high opacity MPC solutions reported here and the low opacity results of GVW is that the latter include radiative energy loss in an Eikonal formalism joined to a parametrized phenomenological “hydrodynamic” component.

It is known that radiative energy loss of ultrarelativistic partons is much larger than elastic energy loss in a medium for a fixed cross section. In GVW a similar quenching pattern was obtained with more modest initial densities  $dN_g/dy \sim 500$  and small pQCD elastic rates because the induced gluon radiation associated with multiple elastic collisions is large enough to compensate for the small elastic transport opacity in that case. In MPC the same level of quenching is achieved only when the elastic opacity is increased artificially by an order of magnitude. Therefore, the present study confirms the expectation that elastic scattering alone is not enough to generate the degree of collectivity observed now at RHIC.

## VI. OUTLOOK

The results presented here underscore the urgent need to develop practical convergent algorithms to incorporate inelastic  $2 \leftrightarrow 3$  processes. Preliminary work in Ref. [18] indicated a rather slow convergence towards Lorentz covariance using the particle subdivision technique. Unlike the  $\ell^{-1/2}$  convergence of  $2 \rightarrow 2$  transport solutions, a much slower rate of convergence  $\propto \ell^{-1/5}$  is expected with the parton subdivision method used to retain Lorentz covariance of  $2 \leftrightarrow 3$  processes.

In addition, a more powerful covariant approximation to Boltzmann transport theory may be needed to overcome the overwhelming computational difficulty in the high opacity regime for central collisions. We found that even for the case of elastic scattering, particle subdivisions up to 1000 are required to maintain covariance and

stabilize the final spectra.

Finally, we note that all results in this paper pertain to slowly varying, smooth initial conditions. In Ref. [29], it was suggested that copious minijet production may induce large (nonstatistical) local fluctuations that could evolve in a turbulent manner. A transport study of differential elliptic flow and jet quenching in such inhomogeneous initial conditions would be interesting to compare to the presently known hydrodynamic and Boltzmann solutions.

## VII. ACKNOWLEDGMENTS

We acknowledge the Parallel Distributed Systems Facility at the National Energy Research Scientific Computing Center for providing computing resources. We also thank RMKI/KFKI for hospitality during the completion of this work.

This work was supported by the Director, Office of Energy Research, Division of Nuclear Physics of the Office of High Energy and Nuclear Physics of the U.S. Department of Energy under contract No. DE-FG-02-93ER-40764. M. G. also was partially supported by Collegium Budapest.

## APPENDIX: COMPARISON OF ELLIPTIC FLOW DEFINITIONS

The main reason that definition (11) gives a very similar elliptic flow to definition (12), contrary to the opposite observation from hydrodynamics, is the difference between the hydro and the cascade  $v_2(b)$  shapes. Hydrodynamical models predict an increasing  $v_2$  out to  $b_m \approx 12 - 13$  fm, while the cascade  $v_2$  peaks at  $b_m \approx 8$  fm. The  $b < b_m$  region where  $v_2$  is small gets a *larger* weight in the STAR definition, while the  $b > b_m$  region where  $v_2$  is as well small gets a *smaller* weight. The former effect tends to reduce elliptic flow, while the latter tends to increase it. In the case of hydrodynamics, the first effect dominates, while for the cascade, the second effect turns out to be larger.

We illustrate this with a simple analytic calculation. The impact parameter dependence of elliptic flow can be fitted with the general form

$$v_2(b) = K \left( \frac{b}{B} \right)^c \left( 1 - \frac{b}{B} \right)^d, \quad (\text{A1})$$

while the particle spectrum is approximately linear in the  $b = 2 - 12$  fm region of interest

$$\frac{dN}{dydp_{\perp}}(b) = C \left( 1 - \frac{b}{B'} \right). \quad (\text{A2})$$

Here the parameters  $K$ ,  $B$ ,  $B'$ ,  $c$ ,  $d$ , and  $C$  in general depend on  $p_{\perp}$ .

It is easy to show that for the above functions definition (11) gives an elliptic flow  $v_2^{av} = 2K \Gamma(c+2)\Gamma(d+1)/\Gamma(c+d+3)$ , while definition (12) yields  $v_2^{STAR} = 6K \Gamma(c+2)\Gamma(d+2)/\Gamma(c+d+4)$ , provided we assume  $B = B'$  and integrate up to  $b_{max} = B$  in both cases. Therefore,

$$\frac{v_2^{STAR}}{v_2^{av}} = \frac{3d+3}{c+d+3}, \quad (\text{A3})$$

which is larger than one, if and only if  $2d > c$ . For our cascade results, the fits to  $v_2(b)$  give  $d/c \sim 0.6 - 1.4$  [ $c(p_\perp) \sim 1.1 - 3.3$ ,  $d(p_\perp) \sim 1.0 - 4.5$ ], therefore we have  $v_2^{STAR}(p_\perp) > v_2^{av}(p_\perp)$ . On the other hand, hydrodynamics gives an approximately linear  $v_2(b)$ , i.e.,  $c = 1$  and  $d = 0$ , which results in  $v_2^{STAR}(p_\perp) < v_2^{av}(p_\perp)$ .

We found essentially the same when taking an exponential fit to  $dN/dp_\perp(b)$  instead of a linear one.

Equation (A3) yields  $v_2^{STAR}/v_2^{av} \sim 1.1-1.5$  for the cascade (depending on  $p_\perp$  and initial conditions). However, in reality  $B'$  is *smaller* than  $B$  (typically  $B' \approx 11 - 13$  fm, while  $B \approx 13 - 16$  fm), which influences  $v_2^{STAR}$ . Furthermore, the upper limit of integration  $b_{max} = 12$  fm is also smaller than  $B$ . This affects primarily  $v_2^{av}$ , through the normalization constant  $1/b_{max}^2$ . The integrals in both definitions are to a large degree insensitive to variations of  $b_{max}$  because the integrands cut off naturally at large  $b$ .

To illustrate these effects, we repeat the previous analytic calculation with  $b_{max} \equiv xB$  for  $v_2^{av}$ , while  $B' \equiv yB$  and  $b_{max} \equiv x'B'$  for  $v_2^{STAR}$ . The integrals yield

$$v_2^{STAR}(x', y) = 6K \frac{y B_{yx'}(c+2, d+1) - B_{yx'}(c+3, d+1)}{y^3 x'^2 (3 - 2x')} \\ v_2^{av}(x) = 2K \frac{B_x(c+2, d+1)}{x^2}, \quad (\text{A4})$$

where  $B_z(a, b) \equiv \int_0^z dt t^{a-1} (1-t)^{b-1}$  is the incomplete beta function. Thus,

$$\frac{v_2^{STAR}(1-x', 1-y)}{v_2^{STAR}(1, 1)} = 1 + \frac{2d-c}{d+1} y + O(x'^2) + O(y^2) \\ \frac{v_2^{av}(1-x)}{v_2^{av}(1)} = 1 + 2x + O(x^{\min\{2, d+1\}}), \quad (\text{A5})$$

i.e., the leading correction to  $v_2^{av}$  comes at first order in  $(b_{max} - B)$ , while the leading correction to  $v_2^{STAR}$  comes at first order in  $(B' - B)$ .

For parameters and initial conditions considered in this study, the corrected formulas (A4) yield  $v_2^{STAR}/v_2^{av} \sim 0.9 - 1.05$  (with  $x' = 1$ ). The uncertainty of  $v_2^{STAR}$  due to the unknown experimental cutoff  $b_{max}$  (i.e.,  $x'$ ) is less than 5%. For the hydro ( $c = 1$ ,  $d = 0$ ), this analysis gives a much smaller ratio  $v_2^{STAR}/v_2^{av} = 3(1-x')(1-y)/4(1-x) \approx 0.75$ .

- [1] H. Stoecker and W. Greiner, Phys. Rept. **137**, 277 (1986)
- [2] J. Ollitrault, Phys. Rev. **D 46**, 229 (1992).
- [3] H. Sorge, Phys. Rev. Lett. **78**, 2309 (1997) [nucl-th/9610026];
- [4] H. Sorge, Nucl. Phys. **A661**, 577 (1999) [nucl-th/9906051].
- [5] S. Voloshin and Y. Zhang, Z. Phys. C **70**, 665 (1996) [hep-ph/9407282]; A. M. Poskanzer and S. A. Voloshin, Phys. Rev. C **58**, 1671 (1998) [nucl-ex/9805001]; S. A. Voloshin and A. M. Poskanzer, Phys. Lett. **B474**, 27 (2000) [nucl-th/9906075].
- [6] P. F. Kolb, U. Heinz, P. Huovinen, K. J. Eskola and K. Tuominen, hep-ph/0103234; P. Huovinen, P. F. Kolb, U. Heinz, P. V. Ruuskanen and S. A. Voloshin, Phys. Lett. B **503**, 58 (2001) [hep-ph/0101136]; P. F. Kolb, P. Huovinen, U. Heinz and H. Heiselberg, Phys. Lett. B **500**, 232 (2001) [hep-ph/0012137]; P. F. Kolb, J. Sollfrank and U. Heinz, Phys. Lett. B **459**, 667 (1999) [nucl-th/9906003].
- [7] L. P. Csernai and D. Rohrlich, Phys. Lett. B **458**, 454 (1999) [nucl-th/9908034].
- [8] D. Teaney, J. Lauret and E. V. Shuryak, nucl-th/0011058.
- [9] B. Zhang, M. Gyulassy and C. M. Ko, Phys. Lett. **B455**, 45 (1999) [nucl-th/9902016].
- [10] E. E. Zabrodin, C. Fuchs, L. V. Bravina and A. Faessler, Phys. Rev. **C63**, 034902 (2001) [nucl-th/0006056], E. E. Zabrodin *et al.*, nucl-th/0104054.
- [11] M. Bleicher and H. Stoecker, hep-ph/0006147.
- [12] X. Wang, nucl-th/0009019.
- [13] M. Gyulassy, I. Vitev and X. N. Wang, Phys. Rev. Lett. **86**, 2537 (2001), [nucl-th/0012092].
- [14] K. H. Ackermann *et al.* [STAR Collaboration], Phys. Rev. Lett. **86**, 402 (2001) [nucl-ex/0009011].
- [15] H. Appelshauser *et al.* [NA49 Collaboration], Phys. Rev. Lett. **80**, 4136 (1998) [nucl-ex/9711001].
- [16] R. J. Snellings [STAR Collaboration], nucl-ex/0104006.
- [17] D. Molnar and M. Gyulassy, Phys. Rev. **C 62**, 054907 (2000) [nucl-th/0005051].
- [18] D. Molnár, in *Proc. of Quark Matter '99 Int. Conf. on Ultra-relativistic Nucleus-Nucleus Collisions*, Torino, Italy, May 10-15, 1999, eds. L. Riccati, M. Masera, E. Vercellin, p. 236c.
- [19] D. Molnar and M. Gyulassy, nucl-th/0102031; D. Molnar and M. Gyulassy, Nucl. Phys. **A** in press, nucl-th/0104018.
- [20] M. Gyulassy and X. Wang, Comput. Phys. Commun. **83**, (1994) 307 [nucl-th/9502021].
- [21] K. J. Eskola, K. Kajantie, P. V. Ruuskanen, and K. Tuominen, Nucl. Phys. **B570**, 379 (2000) [hep-ph/9909456].
- [22] D. Molnár, MPC 1.0.6. This parton cascade code used in the present study can be downloaded from WWW at <http://nt3.phys.columbia.edu/people/molnard>.
- [23] B. Zhang, Comput. Phys. Commun. **109**, 193 (1998) [nucl-th/9709009].
- [24] M. Gyulassy, Y. Pang, and B. Zhang, Nucl. Phys. **A626**, (1997) 999.
- [25] B. Zhang, M. Gyulassy, and Y. Pang, Phys. Rev. C **58**, (1998) 1175 [nucl-th/9801037].



- [26] Y. Pang, RHIC 96 Summer Study, CU-TP-815 preprint (unpublished); Generic Cascade Program (GCP) documentation available at WWW site <http://rhic.phys.columbia.edu/rhic/gcp>.
- [27] *Proc. of Open Standards for Cascade Models for RHIC (OSCAR)*, BNL-64912, June 23-27, 1997, eds. M. Gyulassy and Y. Pang; Source codes and documentation for transport models under the OSCAR standard can be downloaded from the OSCAR WWW site <http://rhic.phys.columbia.edu/rhic/>.
- [28] J. Binnewies, B. A. Kniehl and G. Kramer, *Z. Phys. C* **65**, 471 (1995) [hep-ph/9407347].
- [29] M. Gyulassy, D. Rischke, and B. Zhang, *Nucl. Phys. A* **613** (1997) 397.

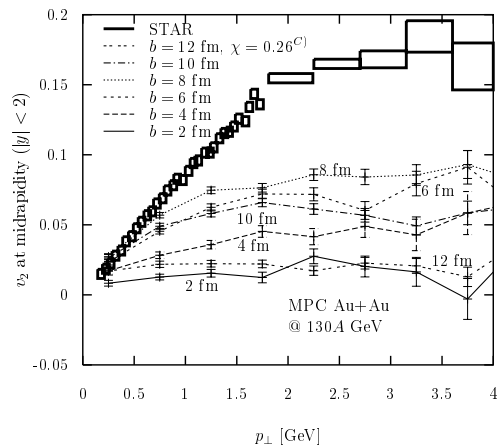


FIG. 1. Gluon elliptic flow as a function of  $p_{\perp}$  for Au+Au at  $\sqrt{s} = 130A$  GeV with impact parameters  $b = 2, 4, 6, 8, 10,$  and  $12$  fm (transport opacities  $\chi = 3.95, 3.49, 2.84, 1.95, 0.99,$  and  $0.26$ ).

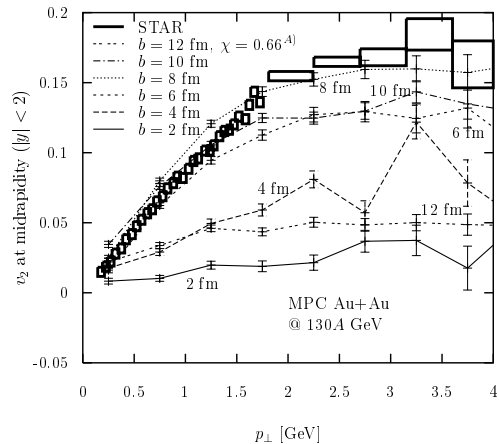


FIG. 2. Gluon elliptic flow as a function of  $p_{\perp}$  for Au+Au at  $\sqrt{s} = 130A$  GeV with impact parameters  $b = 2, 4, 6, 8, 10,$  and  $12$  fm (transport opacities  $\chi = 9.72, 8.61, 7.05, 4.87, 2.50,$  and  $0.66$ ).

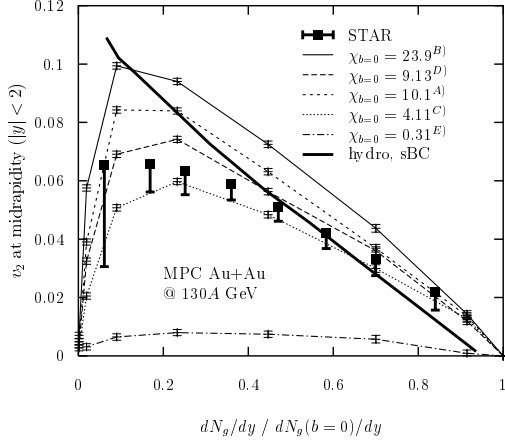


FIG. 3. Gluon elliptic flow as a function of centrality for Au+Au at  $\sqrt{s} = 130A$  GeV with transport opacities  $\chi_{b=0} = 0.31, 4.11, 9.13, 10.1$  and  $23.9$  for  $b = 0$ . Identical to the charged hadron elliptic flow as a function of  $n_{ch}/n_{ch}^{max}$ , if the gluons are hadronized via local parton-hadron duality. The ideal hydrodynamics result is taken from [6] with the so called sBC initial conditions.

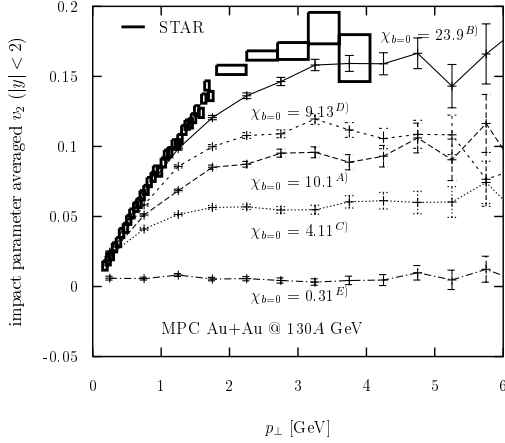


FIG. 4. Impact parameter averaged gluon elliptic flow as a function of  $p_{\perp}$  for Au+Au at  $\sqrt{s} = 130A$  GeV with transport opacities  $\chi_{b=0} = 0.31, 4.11, 9.13, 10.1$  and  $23.9$  for  $b = 0$ . Identical to the charged hadron elliptic flow if the gluons are hadronized via local parton-hadron duality.

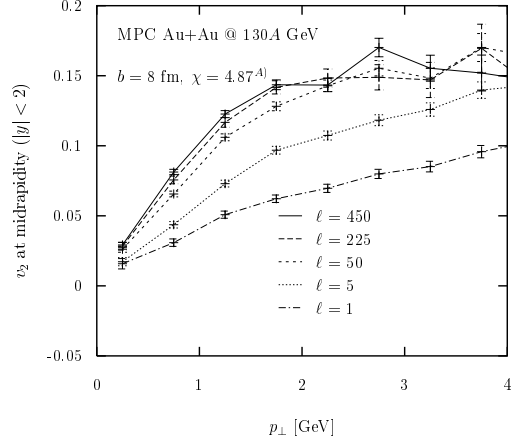


FIG. 5. Gluon elliptic flow as a function of  $p_{\perp}$  for Au+Au at  $\sqrt{s} = 130A$  GeV with  $b = 8$  fm,  $\chi = 4.87$ , and particle subdivisions  $\ell = 1, 5, 50, 225,$  and  $450$ .

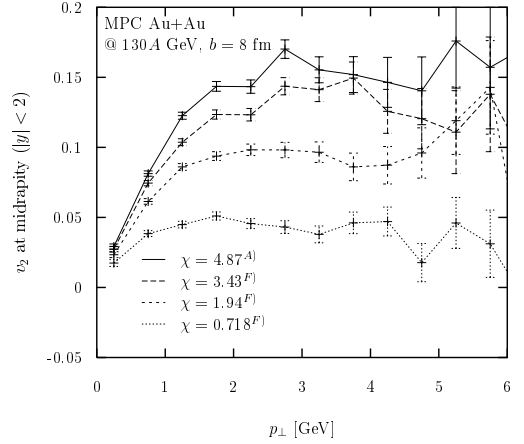


FIG. 6. Gluon elliptic flow as a function of  $p_{\perp}$  for Au+Au at  $\sqrt{s} = 130A$  GeV with  $b = 8$  fm and  $\mu/T_0 = 0.226, 0.45, 0.71,$  and  $1$  ( $\chi = 0.718, 1.94, 3.43,$  and  $4.87$ ).

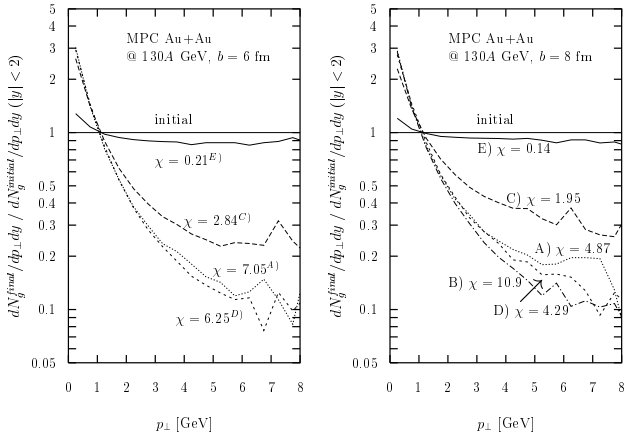


FIG. 7. Final gluon  $p_{\perp}$  spectra relative to the thermal initial spectrum as a function of transport opacity for Au+Au at  $\sqrt{s} = 130A$  GeV with  $b = 6$  fm (left) and  $b = 8$  fm (right). Proportional to the charged hadron  $p_{\perp}$  spectra if the gluons are hadronized via local parton-hadron duality.

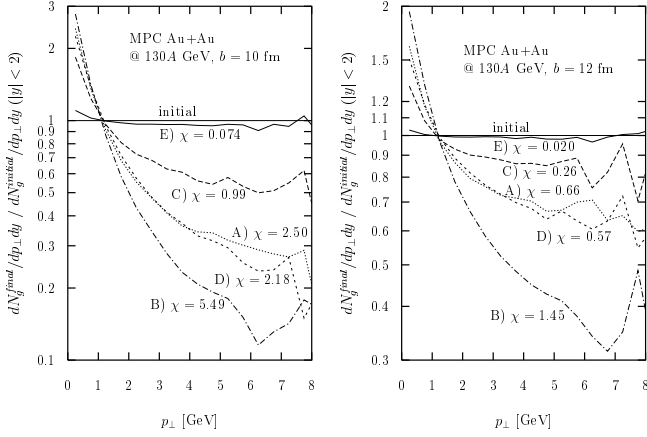


FIG. 8. Same as Fig. 7, except with  $b = 10$  fm (left) and  $b = 12$  fm (right).

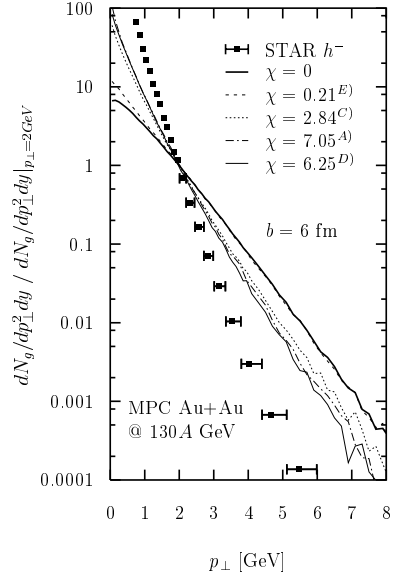


FIG. 9. Same as the curves for  $b = 6$  fm in Fig. 7 but with all curves normalized to 1 at  $p_{\perp} = 2$  GeV. This shows the quenching at high  $p_{\perp}$  relative to  $p_{\perp} = 2$  GeV.

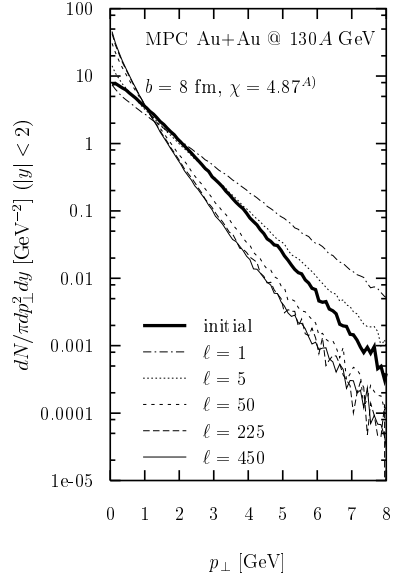


FIG. 10. Final gluon  $p_{\perp}$  spectra for Au+Au at  $\sqrt{s} = 130A$  GeV with  $b = 8$  fm,  $\chi = 4.87$ , and particle subdivisions  $\ell = 1, 5, 50, 225,$  and  $450$ . The spectra are plotted for  $dN(0)/d\eta = 210$ .

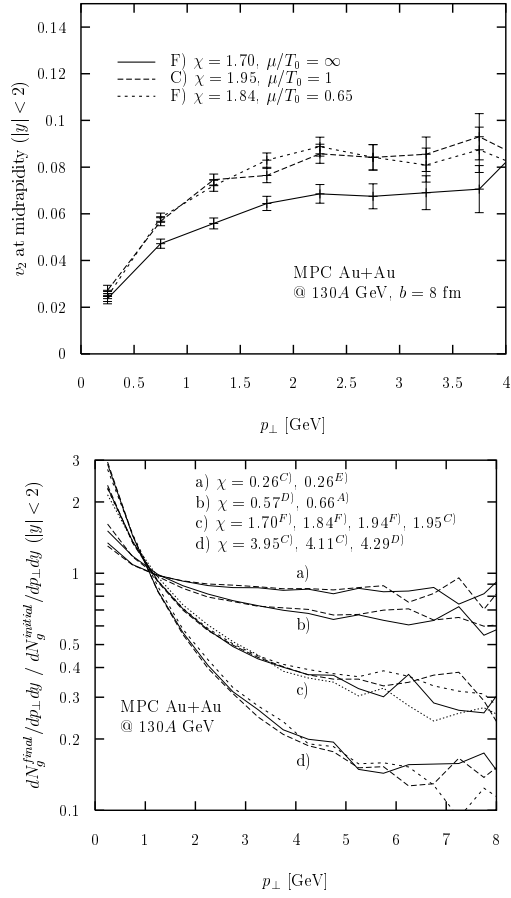


FIG. 11. Transport opacity dependence of gluon elliptic flow and  $p_{\perp}$  spectra.

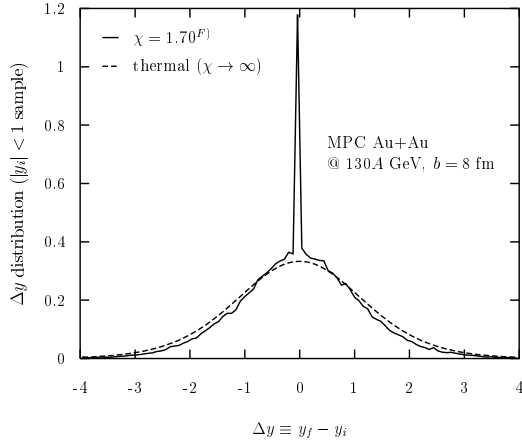


FIG. 12. Correlation between initial and final gluon rapidity.

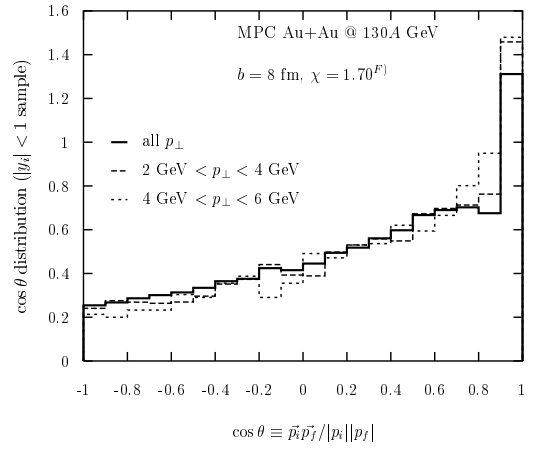


FIG. 13. Correlation between initial and final gluon momentum direction.

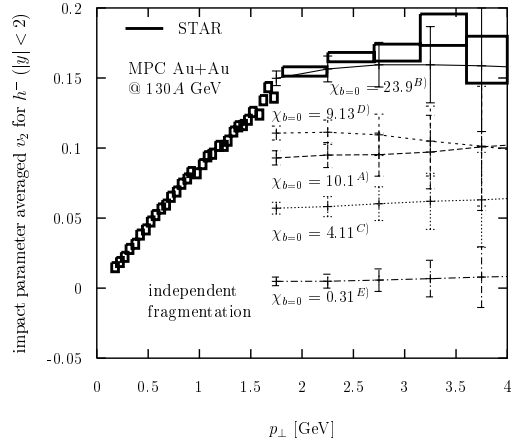


FIG. 14. Impact parameter averaged negative hadron elliptic flow as a function of  $p_{\perp}$  for Au+Au at  $\sqrt{s} = 130A$  GeV with transport opacities  $\chi_{b=0} = 0.31, 4.11, 9.13, 10.1$  and  $23.9$  at  $b = 0$  and hadronization via independent fragmentation. The  $p_{\perp} < 2$  GeV region is not plotted because it is dominated by soft contributions not addressable via pQCD jet fragmentation physics.

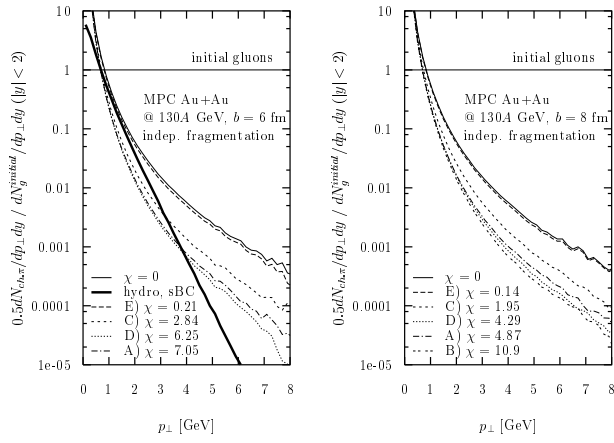


FIG. 15. Final negative hadron  $p_{\perp}$  spectra via independent fragmentation relative to the thermal initial gluon spectrum for Au+Au at  $\sqrt{s} = 130A$  GeV with  $b = 6$  fm (left) and  $b = 8$  fm (right). The ideal hydrodynamics result in the left figure is taken from [6] with the so called sBC initial conditions. It was extrapolated beyond  $p_{\perp} = 3$  GeV using an exponential fit to the  $dN/p_{\perp} dp_{\perp}$  distribution between 2 and 3 GeV.

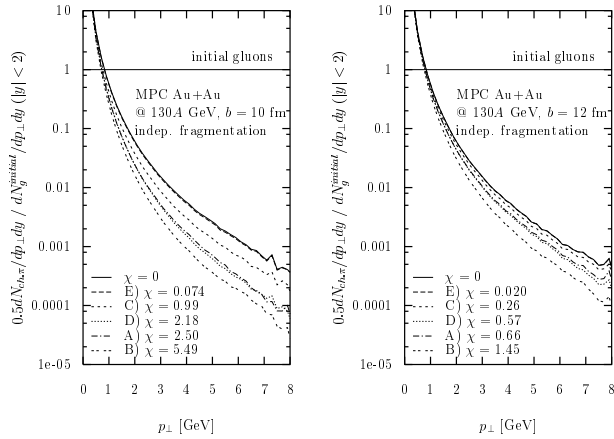


FIG. 16. Same as Fig. 15, except with  $b = 10$  fm (left) and  $b = 12$  fm (right).

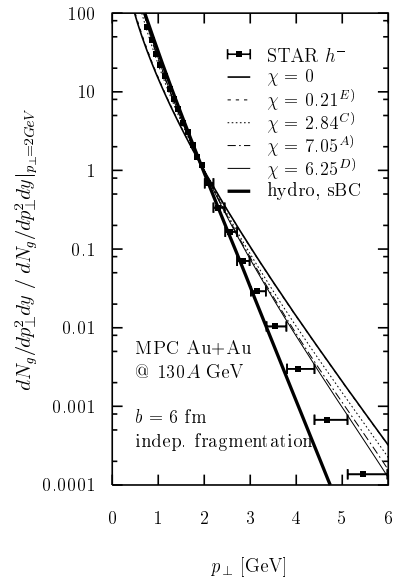


FIG. 17. Same as the curves for  $b = 6$  fm in Fig. 15 but with all curves normalized to 1 at  $p_{\perp} = 2$  GeV. This shows the quenching at high  $p_{\perp}$  relative to  $p_{\perp} = 2$  GeV.

A) $\sigma_0 = 100$ mb, $T_0/\mu = 1$			B) $\sigma_0 = 100$ mb, $T_0/\mu = 0$			
$b$ [fm]	$\langle n \rangle$	$\chi$	$b$ [fm]	$\langle n \rangle$	$\chi$	
0	33.0	10.1	0	35.8	23.9	
2	31.7	9.72	2	34.3	22.9	
4	28.1	8.61	4	30.2	20.1	
6	23.0	7.05	6	24.0	16.0	
8	15.9	4.87	8	16.3	10.9	
10	8.16	2.50	10	8.23	5.49	
12	2.15	0.66	12	2.18	1.45	
C) $\sigma_0 = 40$ mb, $T_0/\mu = 1$			D) $\sigma_0 = 40$ mb, $T_0/\mu = 0$			
$b$ [fm]	$\langle n \rangle$	$\chi$	$b$ [fm]	$\langle n \rangle$	$\chi$	
0	13.4	4.11	0	13.7	9.13	
2	12.9	3.95	2	13.2	8.80	
4	11.4	3.49	4	11.6	7.73	
6	9.26	2.84	6	9.38	6.25	
8	6.37	1.95	8	6.44	4.29	
10	3.23	0.99	10	3.27	2.18	
12	0.86	0.26	12	0.86	0.57	
E) $\sigma_0 = 3$ mb, $T_0/\mu = 1$			F) various, $b = 8$ fm			
$b$ [fm]	$\langle n \rangle$	$\chi$	$\sigma_0$ [fm]	$T_0/\mu$	$\langle n \rangle$	$\chi$
0	1.00	0.31	60	1.54	9.51	1.84
2	0.96	0.29	16	0	2.55	1.70
4	0.85	0.26	100	1.40	15.9	3.43
6	0.69	0.21	100	2.21	15.7	1.94
8	0.47	0.14	100	4.43	15.5	0.718
10	0.24	0.074				
12	0.064	0.020				

TABLE I. Parameters and transport opacity for each transport solution computed via MPC for the present study.